

## Holographic informational properties for a specific Einstein-Maxwell-dilaton gravity theory

Guoyang Fu<sup>1,†</sup>, Peng Liu<sup>2,‡</sup>, Huajie Gong<sup>1,§</sup>, Xiao-Mei Kuang<sup>1,3,||</sup> and Jian-Pin Wu<sup>1,3,\*</sup>

<sup>1</sup>Center for Gravitation and Cosmology, College of Physical Science and Technology, Yangzhou University, Yangzhou 225009, China

<sup>2</sup>Department of Physics and Siyuan Laboratory, Jinan University, Guangzhou 510632, China

<sup>3</sup>School of Aeronautics and Astronautics, Shanghai Jiao Tong University, Shanghai 200240, China



(Received 25 August 2020; accepted 29 June 2021; published 30 July 2021)

We study the holographic information quantities, including the holographic entanglement entropy (HEE), the holographic mutual information (HMI) and the minimum cross section of the entanglement wedge (EWCS), over a special black brane geometry, which has a vanishing ground-state entropy. Thanks to the zero entropy density at the ground state, we expect to extract novel, even singular informational properties in the zero-temperature limit. Surprisingly, we do not observe any singular behavior of entanglement-related physical quantities in the zero-temperature limit. Nevertheless, we find a peculiar property from this model that in the low-temperature region, the HEE decreases with the temperature, which is contrary to that in most holographic models. We argue that this novel phenomenon is brought by the singular property of the zero-temperature limit. In addition, we also compare the features of the information quantities in this special black brane geometry with those in Reissner-Nordstrom anti-de Sitter (RN-AdS) black brane geometry. It is shown that the HEE and HMI of this vanishing ground-state entropy model are always larger than those of RN-AdS geometry, while the EWCS behaves oppositely. Our results indicate that the HMI and EWCS could have different abilities in describing mixed state entanglement.

DOI: [10.1103/PhysRevD.104.026016](https://doi.org/10.1103/PhysRevD.104.026016)

### I. INTRODUCTION

Quantum entanglement is playing an increasingly prominent role in modern physics, from condensed matter theory to the black hole theory. In the context of anti-de Sitter/conformal field theory (AdS/CFT) correspondence [1–4], quantum entanglement also plays a key role in the investigation of how the bulk spacetime emerges from the entanglement structure [5–9]. The entanglement entropy (EE) is a measure of quantum entanglement between two subsystems A and B for a given pure state. In a holographic framework, EE has a simple geometric description known as the Ryu-Takayanagi (RT) formula: that EE for a subregion on the dual boundary is proportional to the minimal surface in the bulk geometry, which is dubbed the

holographic entanglement entropy (HEE) [10–12]. For covariant cases, the RT formula is reformulated into the Hubeny-Rangamani-Takayanagi (HRT) formula [13,14]. Their proposal matches very well with the known results from the two-dimensional CFT [15–17]. The success of the RT/HRT formula has inspired many works toward a better understanding of this topic [18–21] and some important applications. One of the most important applications of HEE is that it can characterize phase transition, including quantum phase transitions and thermodynamic phase transitions; see for instance Refs. [22–30].

However, EE suffers from UV divergence in general, and one has to use a regularization method to remove the divergence. To overcome this regulator-dependent measure of entanglement, a special linear combination of EE called mutual information (MI) was proposed, which is a positive definite quantity guaranteed by the subadditivity and free from the UV divergences [31–33]. In addition, MI removes the thermal entropy contribution [34]. Therefore, MI is a good probe to learn basic properties of any local observable in a quantum system [32,35]. In the holographic framework, one can directly calculate MI with the use of the RT/HRT formula, which is called holographic mutual information (HMI).

It is well known that HEE is a good measure for a bipartite pure state, but it is not suitable for measuring

\*Corresponding author.

jianpinwu@yzu.edu.cn

†FuguoyangEDU@163.com

‡phylp@email.jnu.edu.cn

§huajiegong@qq.com

||xmeikuang@yzu.edu.cn

Published by the American Physical Society under the terms of the [Creative Commons Attribution 4.0 International license](https://creativecommons.org/licenses/by/4.0/). Further distribution of this work must maintain attribution to the author(s) and the published article's title, journal citation, and DOI. Funded by SCOAP<sup>3</sup>.

mixed-state entanglement. In the holographic framework, the minimum cross section of the entanglement wedge (EWCS)  $E_w$  has been associated with the holographic duality of some quantum-information-related physical quantities such as the entanglement of purification (EoP), logarithmic negativity, reflected entropy, and odd entropy [36–42]. The progress shows that EWCS should be closely related to the measures of mixed-state entanglement.

Most of these works (Refs. [36–39]) are implemented in three-dimensional AdS spacetime. For higher-dimensional AdS geometry, we usually resort to numerics. As a first attempt, the authors of Ref. [43] numerically studied the properties of EWCS and its evolution behavior for thermo-field double states dual to the Schwarzschild black hole. Later, in Ref. [44], the authors have developed an algorithm to calculate EWCS for symmetric and asymmetric configurations in pure AdS<sub>4</sub> and four-dimensional Reissner-Nordstrom anti-de Sitter (RN-AdS) black hole backgrounds. The temperature behavior of EWCS and some important inequalities of EWCS are numerically explored. Further, the authors in Ref. [45] studied some holographic informational quantities, including HEE, MI, and EoP, and they argued that the EWCS may be a better entanglement measure of the mixed state than MI. In addition, the connection between EWCS and holographic complexity of purification (CoP) was also explored for various models in Ref. [46].

In this paper, we shall study the information quantities, including HEE, MI, and EWCS, over a type of Einstein-Maxwell-dilaton (EMD) model with a special dilaton potential [47]. For simplicity, here we also refer to this model as Gubser-Rocha model as Refs. [48,49]. The black brane solution of the Gubser-Rocha model possesses two important and appealing characteristics—i.e., zero ground-state entropy density and linear specific heat at low temperature, which are also the characteristics of a Fermi gas. The study of the probe fermionic spectrum over the Gubser-Rocha model also confirms that the system shares the same property of the degenerate Fermi liquid [50,51]. Some interesting studies based on the Gubser-Rocha model have also been implemented; see Refs. [23,52,53] and references therein. In particular, in Ref. [52], the ionic lattice background in the framework of the Gubser-Rocha model was constructed, and the optical conductivity of the dual field theory on the boundary was studied. In addition, some of us constructed a Q-lattice deformed Gubser-Rocha model with vanishing ground entropy density, over which the HEE was explored, and it was claimed that the first-order derivative of HEE with respect to Q-lattice parameters could characterize the quantum phase transition [23].

In contrast with RN-AdS geometry, which has a non-vanishing ground-state entropy density, the Gubser-Rocha model provides a novel platform to study the holographic

phenomena. Here, we aim to study the universal properties of HEE, MI, and EWCS over the Gubser-Rocha model, and to compare the results from such a model with vanishing ground-state entropy density with those from RN-AdS geometry studied in Ref. [44].

Our paper is organized as follows. In Sec. II, we present a brief review of the Gubser-Rocha model. Then, we numerically calculate the HEE, MI, and EWCS and discuss the novel properties of these holographic informational quantities in Sec. III. Conclusions and discussions are presented in Sec. IV.

## II. GUBSER-ROCHA MODEL

We start with the following action [47,54]:

$$S = \frac{1}{2\kappa^2} \int d^4x \sqrt{-g} \left[ R - \frac{1}{4} e^\Phi F^{\mu\nu} F_{\mu\nu} - \frac{3}{2} (\partial_\mu \Phi)^2 + \frac{6}{L^2} \cosh \Phi \right], \quad (1)$$

where  $L$  is the AdS radius,  $\Phi$  is the dilation field, and  $F_{ab} = \partial_a A_b - \partial_b A_a$ . An analytical charged black brane solution to the above action has previously been given in [47]

$$ds^2 = \frac{L^2}{z^2} \left( -f(z) dt^2 + \frac{dz^2}{f(z)} + g(z)(dx^2 + dy^2) \right), \quad (2)$$

$$A_t(z) = L \sqrt{3Q} (1-z) \frac{\sqrt{1+Q}}{1+Qz}, \quad (3)$$

where

$$f(z) = (1-z) \frac{p(z)}{g(z)}, \quad g(z) = (1+Qz)^{3/2},$$

$$p(z) = 1 + (1+3Q)z + (1+3Q(1+Q))z^2. \quad (4)$$

The coordinate system we take is labeled the same as that in Ref. [52], which is the coordinate transformation based on the solution presented in Ref. [47]. In our current coordinate system, the Hawking temperature can be worked out as

$$\hat{T} = \frac{3\sqrt{1+Q}}{4\pi L}. \quad (5)$$

The system is determined by the scaling invariant temperature

$$T = \frac{\hat{T}}{\mu} = \frac{\sqrt{3}}{4\pi L \sqrt{Q}}, \quad (6)$$

where  $\mu$  is the chemical potential in the dual boundary field theory, and it is related to the parameter  $Q$  as

$$\mu = \sqrt{3Q(1+Q)}. \quad (7)$$

The temperature  $T$  is inversely proportional to the parameter  $Q$ . When  $Q$  tends to zero, it goes up to infinity, and the black brane is a Schwarzschild-AdS black brane. As  $Q$  approaches infinity, it goes down to zero, which corresponds to an extremal black brane.

It is worthwhile to emphasize that this black brane geometry possesses an appealing characteristic—i.e., the zero ground-state entropy, in contrast to the usual RN-AdS black brane, which has finite entropy density even at zero temperature. For more discussion on the thermodynamics of this charged black brane, please refer to Ref. [47].

In the high-temperature limit, the geometry of the Gubser-Rocha model and the RN-AdS model are the same. This can be seen by taking the  $Q \rightarrow 0$  limit for the Gubser-Rocha model and the  $\mu \rightarrow 0$  limit for the RN-AdS model. It predicts that all the information-related quantities will be the same. As long as the quantities related to quantum information are only related to the background geometry, we can conclude that the quantum information behavior of the Gubser-Rocha model is consistent with that of the RN-AdS model in the high-temperature limit. Therefore, we pay more attention to their finite-temperature and extremely low-temperature behavior.

### III. THE HOLOGRAPHIC INFORMATION-RELATED QUANTITIES

In this section, we shall study the holographic information-related quantities over the Gubser-Rocha model. In order to demonstrate the peculiar properties of the holographic information quantities over the Gubser-Rocha model, we shall also present the corresponding results from a RN-AdS black brane for comparison throughout this paper. For RN-AdS black brane geometry, we refer to Ref. [44].

#### A. Holographic entanglement entropy

EE, as a measure of entanglement, is one of the hot topics in quantum information. For a pure-state system composed of two parts A and B, its EE is described by von Neumann entropy  $S_A \equiv -\text{Tr}(\rho_A \ln \rho_A)$ , where  $\rho_A \equiv \text{Tr}_B |\psi\rangle\langle\psi|$ . Holographically, the von Neumann entropy can be depicted through the R-T formula as [10]

$$S_A = \frac{\text{Area}(\gamma_A)}{4G_N}, \quad (8)$$

where  $G_N$  is the bulk Newton constant.  $\gamma_A$  is the minimal surface which stretches into the bulk and ends at  $\partial A$ .

We consider a specific configuration in which the subsystem A is an infinite strip along the  $y$  axis with width  $l$  along the  $x$  axis—i.e.,  $A := \{0 < x < l, -\infty < y < \infty\}$  (see Fig. 1). Since the minimum surface is invariant along

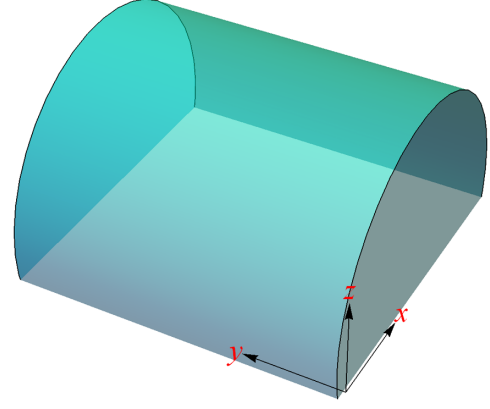


FIG. 1. Diagram of the extremal surface for an infinite strip configuration with width  $l$ .

the  $y$  axis, it is convenient to describe this minimum surface by the radial coordinate  $z(x)$ . When we fix the width, the HEE can be explicitly expressed as

$$\hat{S} = 2 \int_{\epsilon}^{z_*} dz \frac{g(z)^{\frac{3}{2}}}{z^2 \sqrt{f(z)(g(z)^2 - \frac{z^4}{z_*^4} g(z_*)^2)}}, \quad (9)$$

$$\hat{l} = 2 \int_{\epsilon}^{z_*} dz \frac{g(z_*)}{\sqrt{f(z)g(z) \sqrt{\frac{z_*^4 g(z)^2}{z^4} - g(z_*)^2}}}, \quad (10)$$

where  $z_*$  is the top (alternatively called the turning point) of the minimum surface. Since the HEE is divergent at the asymptotic AdS boundary, we have introduced a cutoff  $\epsilon$  in the above expression. To subtract out the vacuum contribution to the HEE, we add a counterterm  $-1/z^2$  into the integration of  $\hat{S}$ , such that we have the regularized HEE as what follows:

$$\hat{S} = 2 \left( \int_{\epsilon}^{z_*} \left( \frac{g(z)^{\frac{3}{2}}}{z^2 \sqrt{f(z)(g(z)^2 - \frac{z^4}{z_*^4} g(z_*)^2)}} - \frac{1}{z^2} \right) dz - \frac{1}{z_*} \right). \quad (11)$$

Note that here  $\hat{l}$  and  $\hat{S}$  are the dimensionful width and HEE. Adopting  $\mu$  as the scaling unit, we have the scaling-invariant width and HEE, which are  $l \equiv \hat{l}\mu$  and  $S \equiv \hat{S}/\mu$ . We shall only focus on the scaling-invariant quantities in the following study.

Before showing the behaviors of HEE, we first study the behaviors of the turning point  $z_*$ , which are exhibited in Fig. 2. It is easy to find that there are some obvious differences between the behaviors of  $z_*$  for the Gubser-Rocha model and RN-AdS geometry. We summarize the differences and similarities between them as what follows:

- (1) In the high-temperature region,  $z_*$  as the function of width  $l$  shares similar behavior for the Gubser-Rocha model and RN-AdS geometry. That is to

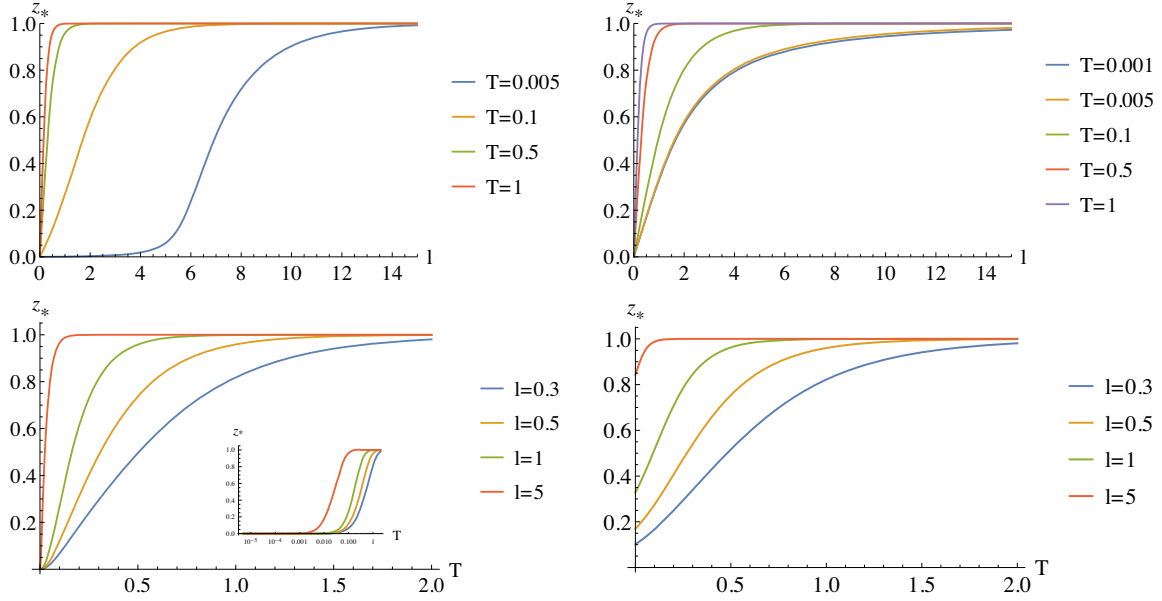


FIG. 2. The turning point  $z_*$  as the function of width  $l$  for fixed temperature (plots above) and as the function of temperature  $T$  for fixed  $l$  (plots below). The left plots show the case for the Gubser-Rocha model, and the right plots for the RN-AdS background.

say,  $z_*$  monotonically increases as  $l$  increases. When  $l \rightarrow \infty$ ,  $z_*$  approaches the horizon of the black hole, while in the limit of  $l \rightarrow 0$ ,  $z_* \rightarrow 0$ . It is expected that in the high-temperature limit, as we have mentioned in the above subsection, the  $z_*$  and many information-related quantities of the Gubser-Rocha model are similar to those of the RN-AdS model.

- (2) However, in the low-temperature region,  $z_*$  exhibits some obvious differences between the Gubser-Rocha model and RN-AdS geometry. From the top-left plot of Fig. 2, we see that for the Gubser-Rocha model, there is a domain of  $l$  where  $z_*$  is almost zero. As  $l$  increases and passes beyond some critical value,  $z_*$  gradually climbs up and finally approaches the black hole horizon. But for the RN-AdS geometry, there is no such domain of  $l$  (see the top-right plot). Correspondingly, for the Gubser-Rocha model, there is a domain of  $T$  where  $z_*$  almost vanishes (see the lower-left plot of Fig. 2) when  $l$  is smaller than some critical value. But conversely, for a RN-AdS background,  $z_*$  is finite for nonzero  $l$  in the limit of zero temperature (see the lower-right plot). In the low-temperature region of the Gubser-Rocha model, it is seen that for a fixed width  $l$ , one has  $\hat{l} = l/\mu \rightarrow 0$ , which means that the minimum surface will only stay at the near boundary region. This explains why  $z_*$  for the Gubser-Rocha model is significantly smaller than that for the RN-AdS model in the low-temperature region.

We would like to point out that to find the difference of  $z_*$  between the Gubser-Rocha model and RN-AdS

background, we have implemented a numerical computation with higher precision. This is not an easy and straightforward work, because in the limit of zero temperature,  $z_*$  for the Gubser-Rocha model also tends to zero, such that much higher precision and precaution are needed in the numerics. In addition, in the following numerical calculations, the numerical precision depends crucially on the precision of the  $z_*$  value.

We move on to study the behaviors of HEE. The HEE as a function of width  $l$  for fixed temperature and as a function of temperature  $T$  for fixed  $l$  are exhibited in Fig. 3. Qualitatively, the behaviors of HEE for the Gubser-Rocha model are similar to those for a RN-AdS background. That is to say, for fixed and finite temperature, as the width  $l$  decreases, the HEE decreases and tends to negative infinity in the limit of  $l \rightarrow 0$ , while for fixed width  $l$ , as the temperature rises, the HEE increases. However, if we take a closer look at the relation between the temperature and the HEE, we find that in the high-temperature region, the values of HEE for the Gubser-Rocha model and the RN-AdS background are almost the same. But in the low-temperature region, the HEE for the Gubser-Rocha model is larger than that for the RN-AdS background. It means that the degree of freedom in the Gubser-Rocha model is more entangled than that in the RN-AdS model in the low-temperature region.

Further, in more detail, we compare the Gubser-Rocha model and the RN-AdS model with different widths in Fig. 4. We find that the HEE of the Gubser-Rocha model in the low-temperature region exhibits a nonmonotonic

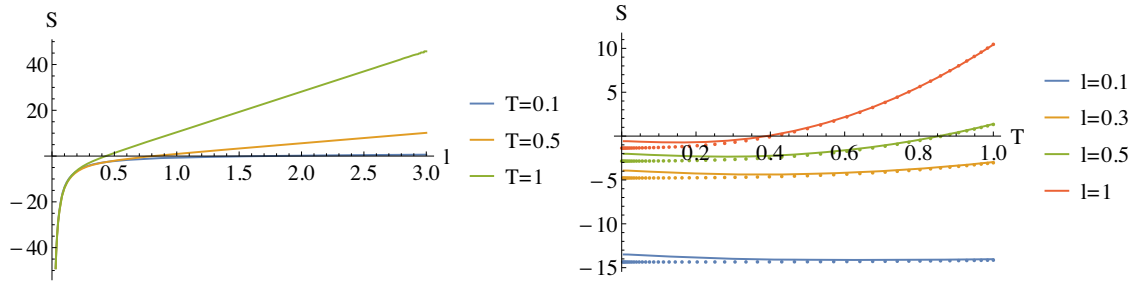


FIG. 3. HEE as a function of the width  $l$  for fixed temperature (left plot), and as a function of temperature  $T$  for fixed  $l$  (right plot). The solid lines are for the Gubser-Rocha model, and the dotted lines are for the RN-AdS background.

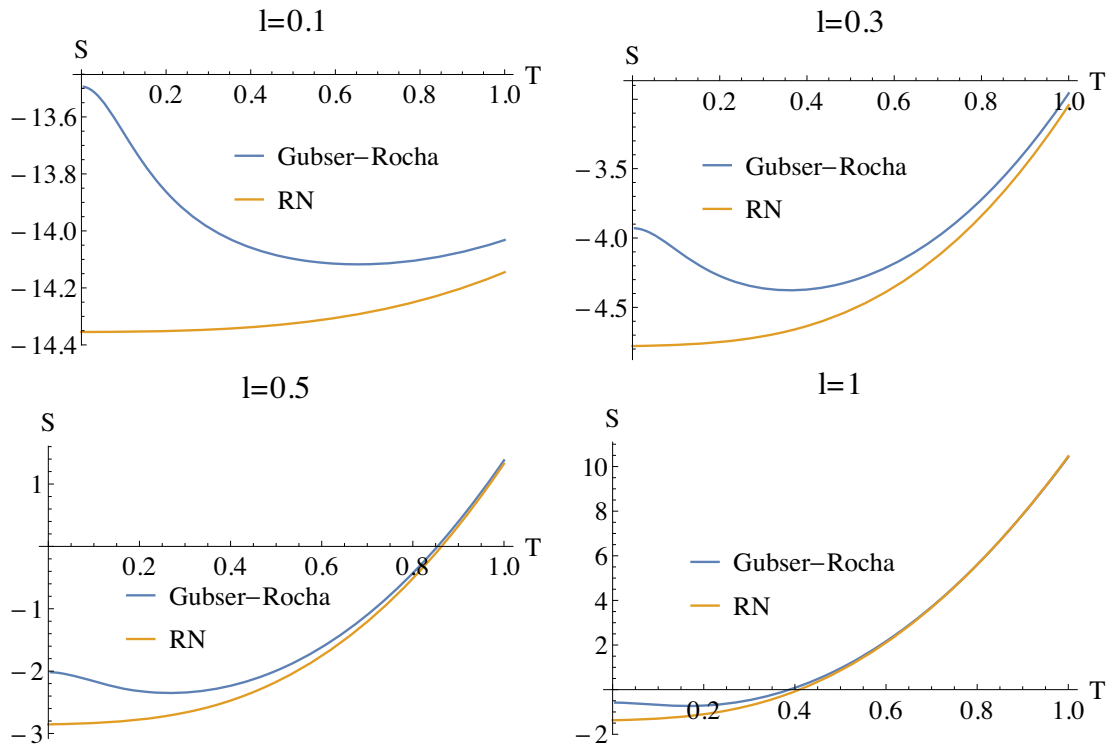


FIG. 4. HEE as a function of the temperature for different widths  $l$ . The blue line is for the Gubser-Rocha model, and the orange line is for the RN-AdS background.

behavior such that the HEE decreases first and then increases with the increase of the temperature. This is in contrast to the case of the Gubser-Rocha model, for which the HEE for the RN-AdS background increases as the temperature goes up even in the region of low temperature. For a detailed analysis for the case of a RN-AdS background, we can refer to Ref. [44]. Another interesting property of the Gubser-Rocha model is that the HEE seems to flatten out at extremal low temperatures (Fig. 4). For this peculiar behavior, we shall give some analytical understanding in what follows.

In the case of the RN-AdS model in Ref. [44], we can analytically obtain the expression of the HEE at low temperature by expanding the HEE with  $z \rightarrow 0$ . However, the expansion is valid only if any other quantity is finite compared with  $z$ . For the Gubser-Rocha model, there are two limits when implementing the analytical deduction. The first one is the zero-temperature limit  $Q \rightarrow \infty$  for  $T \rightarrow 0$ . The second one is  $z \rightarrow 0$  for any minimum surface with finite width, since  $\mu \rightarrow \infty$  will render a small dimensional width  $\hat{l}$ . Given the above two limits, one cannot expand with  $z \rightarrow 0$  or  $Q \rightarrow \infty$  solely.

Assuming that  $Q_z$  and  $Q_x$  are finite, the expression of the area reads

$$\begin{aligned} S &= \frac{1}{\mu} \int_C \sqrt{g_{yy}} \sqrt{g_{xx} dx^2 + g_{zz} dz^2} \\ &= \int_C \frac{1}{z^2} \sqrt{\frac{(Qz+1)^3}{3Q(Q+1)}} \sqrt{dx^2 + \frac{dz^2}{(1-z)(1+z+3Qz+z^2+3Qz^2+3Q^2z^2)}}, \end{aligned} \quad (12)$$

where  $\int_C$  indicates the integral of the line element along the geodesic. Now, we rescale the coordinate with  $\tilde{z} \equiv Qz$ ,  $\tilde{x} \equiv Qx$ , and this results in

$$\begin{aligned} S &= \int_C \frac{\sqrt{(\tilde{z}+1)^3 \left( d\tilde{x}^2 - \frac{d\tilde{z}^2}{(\frac{\tilde{z}}{Q}-1)(\frac{\tilde{z}^2}{Q^2} + \frac{3\tilde{z}^2}{Q} + \frac{\tilde{z}}{Q} + 3\tilde{z}^2 + 3\tilde{z} + 1)} \right)}}{\sqrt{3} \sqrt{\frac{1}{Q} + 1\tilde{z}^2}} \\ &= \int_C \frac{1}{\tilde{z}^2} \sqrt{\frac{(\tilde{z}+1)^3}{3(\frac{1}{Q} + 1)}} \sqrt{d\tilde{x}^2 - \frac{d\tilde{z}^2}{(\frac{\tilde{z}}{Q}-1)(\frac{\tilde{z}^2}{Q^2} + \frac{3\tilde{z}^2}{Q} + \frac{\tilde{z}}{Q} + 3\tilde{z}^2 + 3\tilde{z} + 1)}} \\ &= S_0 + \frac{S_1}{Q} + \mathcal{O}(Q^{-2}), \end{aligned} \quad (13)$$

with

$$S_0 = \int_C \left( \frac{\sqrt{(\tilde{z}+1)^3}}{\sqrt{3}\tilde{z}^2} \sqrt{d\tilde{x}^2 + \frac{d\tilde{z}^2}{3\tilde{z}^2 + 3\tilde{z} + 1}} \right), \quad (14)$$

$$S_1 = - \int_C \frac{\sqrt{(\tilde{z}+1)^3} \left( \frac{-3\tilde{z}^3 + 3\tilde{z}^2 + 3\tilde{z} + 1}{(3\tilde{z}^2 + 3\tilde{z} + 1)^2} z'(x)^2 + 1 \right)}{2\sqrt{3}\tilde{z}^2 \sqrt{\frac{z'(x)^2}{3\tilde{z}^2 + 3\tilde{z} + 1} + 1}} d\tilde{x}. \quad (15)$$

We expand  $S$  up to the second order of  $1/Q$ . The leading term  $S_0$  is a constant depending on the specific value of the width. The subleading term follows  $S_1/Q \sim T^2$ . Therefore, we have

$$S = S_0 + S_1 T^2 + \mathcal{O}(T^4). \quad (16)$$

This explains the flat behavior of  $S$  vs  $T$  in the zero-temperature limit, since  $\partial_T S|_{T \rightarrow 0} = 0$ . Obviously, the  $S$  in the zero-temperature limit only involves even orders of  $T$ , since it can be expanded with  $1/Q$ . When the width is small and satisfies  $\tilde{z} \leq 1.70241$  such that  $-3\tilde{z}^3 + 3\tilde{z}^2 + 3\tilde{z} + 1 > 0$ , we can find from Eq. (15) that  $S_1 < 0$ , and hence the decreasing behavior between  $S$  and  $T$  can be proved. However, for  $\tilde{z}$  outside this region, so far we cannot determine the monotonicity analytically.

Further, we improve the numerical precision such that we can obtain the HEE at the extremal low temperature (the red dots in Fig. 5). Using the command FindFit in

*Mathematica*, we can give the optimal fitted results, which are shown in Fig. 5 (blue lines). The power exponent  $\delta \simeq 2$  (Table I). This verifies the analytical result [Eq. (16)].

In addition to the relation between HEE and the temperature, another interesting scaling relation between  $z_*$  and the temperature can also be deduced from Eq. (13). Noticing that the leading term of Eq. (13) only involves  $\tilde{z} \equiv Qz$ , one finds that  $S$  is invariant under the following rescaling:

$$Q \rightarrow Q/\xi, \quad z \rightarrow \xi z, \quad x \rightarrow \xi x, \quad \mu \rightarrow \mu/\xi, \quad (17)$$

where  $\xi$  is a constant. Therefore, given a minimum surface  $z(x)$  at width  $l$ , we can directly derive that the rescaling of the solution  $\tilde{z}(\tilde{x}) = \xi z(\xi x)$  is still a minimum surface. Now, we arrive at the conclusion that

$$z_* \sim 1/Q \sim T^2. \quad (18)$$

We also numerically verify the above analytical results. Figure 6 shows the turning point  $z_*$  as a function of the temperature  $T$  for different  $l$  in double-log coordinates. We see that  $z_*$  linearly decreases with the temperature in these double-log coordinates. Further, by numerical fitting, we find that the power exponent  $\gamma \simeq 2$  for different  $l$  (see Table II). Therefore, we confirm the robustness of the temperature behavior of  $z_*$ .

To summarize, the HEE of the Gubser-Rocha model exhibits some interesting peculiar behaviors—for example,

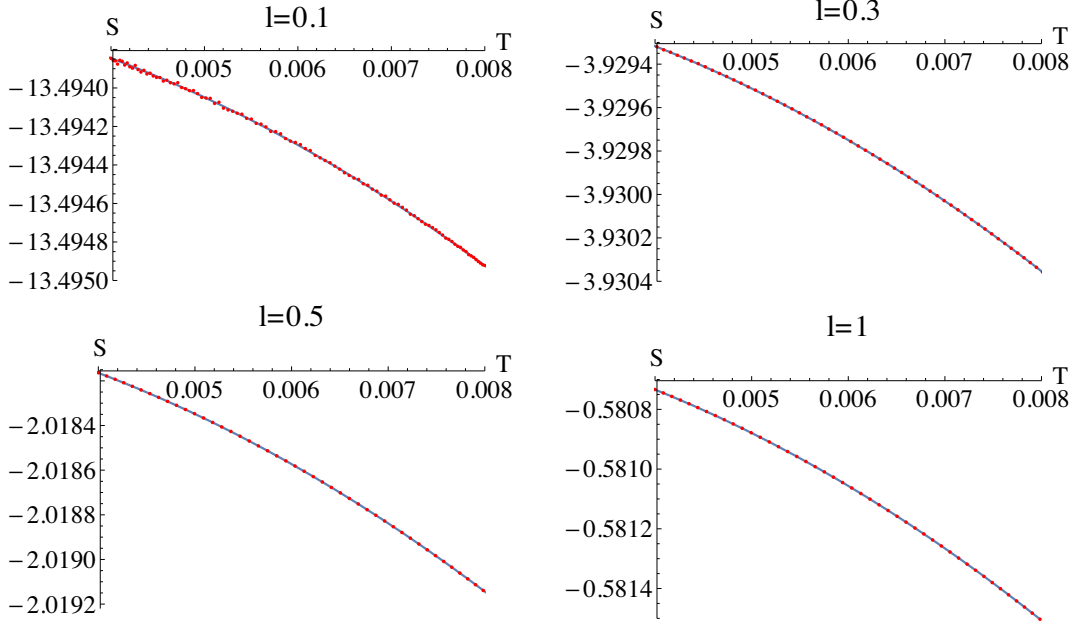


FIG. 5. The HEE at extremal low temperature for different widths  $l$ . The red dots are the numerical results, while the blue solid lines are fitted by the formula  $\alpha + \beta T^\delta$ . Here,  $\alpha$ ,  $\beta$ , and  $\delta$  are the constants.

TABLE I. The HEE behaviors can be fitted by the formula  $\alpha + \beta T^\delta$ . Using the command `FindFit` in *Mathematica*, we can give the optimal fitted results, which give the power exponent  $\delta \simeq 2$ .

$l$	0.1	0.3	0.5	1
$\delta$	1.969	1.992	1.994	1.994

nonmonotonic behavior at low temperatures and then flattening-out behavior in the zero-temperature limit. These peculiar properties can be attributed to the singular property of the Gubser-Rocha model in the limit of zero temperature. As far as we know, it has not been reported elsewhere. There are other models exhibiting vanishing entropy density at zero temperature; for example, see Refs. [55,56], where the background solution is numerically constructed. It shall

TABLE II. We fit the temperature behavior of the turning point  $z_*$ . The fit function is  $z_* \sim T^\gamma$ . The power exponent  $\gamma \simeq 2$  for different  $l$ , which is in agreement with the analytical result in Eq. (18).

$l$	0.1	0.3	0.5	0.7	1
$\gamma$	2.0000	1.9997	2.0000	2.0000	2.0000

be interesting to further explore the HEE behavior at low temperature over this background geometry [55,56].

## B. Mutual information

In this subsection, we study the mutual information (MI) from the Gubser-Rocha model. HEE suffers from the divergence from the asymptotic AdS boundary, and so we need to introduce a cutoff, just as was done as the previous subsection. This issue can be avoided in MI.

To proceed, we consider two disjoint subsystems  $A$  and  $C$ , which are separated by the subsystem  $B$ . Then, the MI between  $A$  and  $C$  can be defined as

$$I(A, C) = S_A + S_C - S_{A \cup C}. \quad (19)$$

A non-trivial MI requires  $S(A \cup C) = S(B) + S(A \cup B \cup C)$ . Obviously, MI is a linear combination of EE. Due to this appropriate combination, the UV divergence of HEE is removed in MI. In addition, MI partly removes the thermal entropy contribution [34]. Therefore, it is a more relevant quantity to describe quantum entanglement.

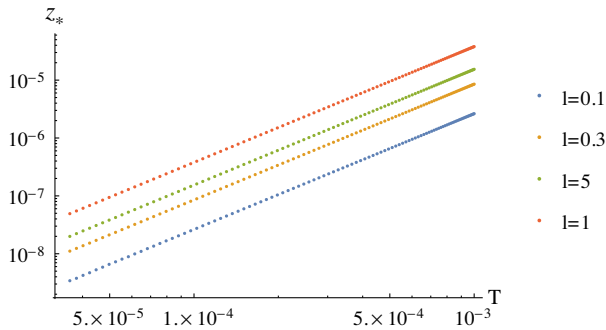


FIG. 6. The turning point  $z_*$  versus temperature  $T$  in double-log coordinates.

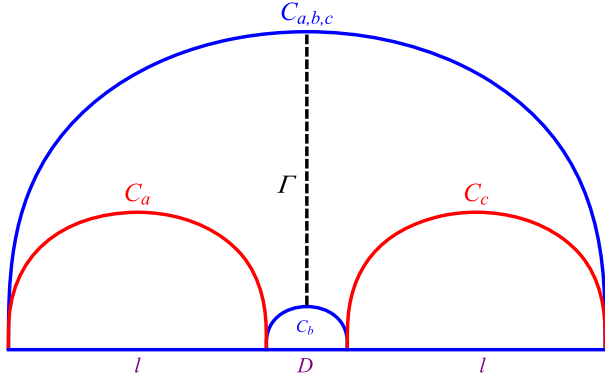


FIG. 7. A diagram of MI and  $E_w$  for symmetric configuration. A nontrivial MI equals the difference between the area of connected configuration (blue curves) and the area of the disconnected configuration (red curves). The vertical dashed line  $\Gamma$  represents the minimal cross section connecting the tops of  $C_b$  and  $C_{a,b,c}$ .  $l$  denotes the size of the subsystems, and  $D$  is the separation scale.

We again consider an infinite strip configuration along the  $y$  axis for the subsystems and focus on the symmetric case, which is described as

$$\begin{aligned} A &:= \{0 < x < l, -\infty < y < \infty\}, \\ B &:= \{l < x < l + D, -\infty < y < \infty\}, \\ C &:= \{l + D < x < 2l + D, -\infty < y < \infty\}. \end{aligned} \quad (20)$$

$l$  is the size of the subsystem, and  $D$  is the separation scale. The intersecting surface of this configuration is shown in Fig. 7.

The left plot in Fig. 8 exhibits MI over the Gubser-Rocha model as a function of the separation scale  $D$  for fixed subsystem size  $l$  and different temperatures (solid lines). We find that for fixed temperature and subsystem size  $l$ , MI decreases as the separation scale  $D$  increases. If we further increase the separation scale such that it is beyond a certain critical value, MI vanishes, which indicates disentangling

between two subsystems. We also exhibit the behavior of MI as a function of the system size  $l$  for fixed  $D$  and different temperatures in the right plot in Fig. 8. We find that MI decreases with the decrease of  $l$  and vanishes when  $l$  is below some value. This result is qualitatively in agreement with that over a neutral black hole [34] and also over a RN-AdS background (dotted lines). But note that quantitatively, the value of MI over RN-AdS is smaller than that over the Gubser-Rocha model. Further, Fig. 9 shows the parameter space  $(l, D)$ , in which the shaded region denotes nonzero MI. An obvious characteristic is that for the fixed temperature, when the subsystem size  $l$  increases, the critical lines tend to be a constant. It indicates that if we want to have a nonzero MI, the separation scale  $D$  shall be constrained in a certain region.

In addition, we also note that the MI of the Gubser-Rocha model is always larger than that of the RN-AdS model. This observation is consistent with that of the HEE, which has been found in the above section. This consistency is reasonable, because the MI is directly related to the HEE. It would be interesting to test whether another entanglement measure, the EWCS, would give the same behavior. We shall discuss this question in the next subsection.

In the left plot in Fig. 10, we show the result of how MI depends on the temperature for the Gubser-Rocha model (solid lines). We see that as the temperature rises, MI falls and finally vanishes when the temperature is beyond some critical value. Therefore, when we heat up the system, a disentangling transition happens. This observation is consistent with that in Refs. [34,57]. To make a comparison, we also show MI as a function of the temperature over a RN-AdS background (dotted lines in Fig. 10). We again confirm that the value of MI over a RN-AdS background is smaller than that over the Gubser-Rocha model.

In the above study, we consider that the configuration is symmetric—i.e., the sizes of the subsystems  $A$  and  $C$  are equal. Next, we turn to explore the properties of MI with nonsymmetrical configuration—i.e., the sizes of  $A$  and  $C$  are unequal, as shown in Fig. 11. We denote the sizes of the

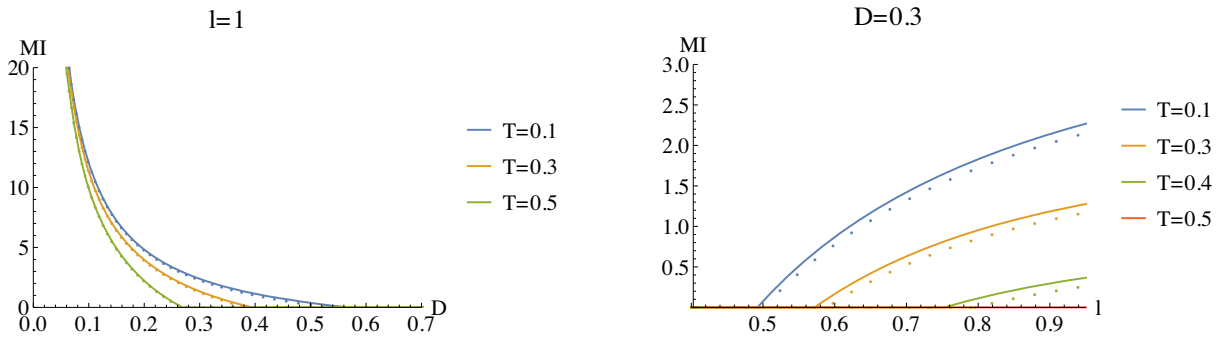


FIG. 8. Left plot: MI as a function of separation scale  $D$  with fixed system size  $l$  for different temperatures. Right plot: MI as a function of system size  $l$  with fixed separation scale  $D$  for different temperatures. The solid lines are for the Gubser-Rocha model, and the dotted lines are for the RN-AdS background.

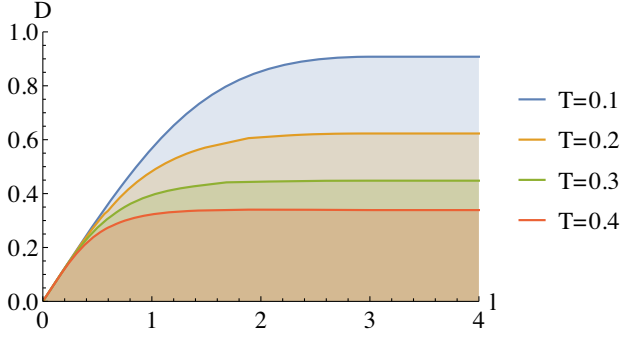


FIG. 9. Parameter space  $(l, D)$ , in which MI is nonzero only in the shaded region.

subsystems  $A$  and  $C$  as  $a$  and  $c$  and the separation size as  $b$ . Figure 12 exhibits MI as a function of the temperature over the Gubser-Rocha model for a nonsymmetrical configuration. Qualitatively, the picture of MI for a nonsymmetrical configuration is consistent with that for symmetrical configuration. In particular, the value of MI over RN-AdS geometry is also smaller than that over the Gubser-Rocha model, which indicates that this behavior is robust and independent of the configuration.

Finally, we also see the difference  $\delta MI$  as the function of  $T$  between the Gubser-Rocha model and the RN-AdS

background, which is shown in the insets in Figs. 10 and 12. For most configurations, as the temperature rises,  $\delta MI$  first increases, and then decreases when the temperature further rises. Therefore, for these configurations, the MIs of the Gubser-Rocha and AdS-RN models approach one another at high temperatures. This picture is consistent with that of HEE and  $E_w$ , which shall be studied in the next subsection. However, we would like to point out that for some configurations—for example,  $l = 0.6$  in the right plot of Fig. 10 and  $a = 0.5, b = 0.3, c = 1$  in the right plot of Fig. 12—we cannot see the turning point of the temperature, after which  $\delta MI$  decreases as the temperature rises. This is because, as the temperature is increased beyond some critical temperature, there is a disentangling phase transition that MI reduces to zero.

### C. Minimum cross section of the entanglement wedge

In this subsection, we turn to explore  $E_w$  over the Gubser-Rocha model [36,37]. We first study the case of symmetric configuration, for which the EWCS equals the area of the vertical line  $\Gamma$  connecting the tops of the minimum surfaces (see Fig. 7). The EWCS over the Gubser-Rocha model can be specifically calculated as

$$\begin{aligned} \Gamma &= \int_{z_D}^{z_{2l+D}} \sqrt{g_{yy}g_{zz}} dz \\ &= \int_{z_D}^{z_{2l+D}} \frac{(16\pi^2 \hat{T}^2 + 3z)^{3/2}}{4\pi \hat{T} z^2 \sqrt{27(z-1)z^2 + 144\pi^2 \hat{T}^2 z(z^2-1) + 256\pi^4 \hat{T}^4 (z^3-1)}} dz. \end{aligned} \quad (21)$$

We then numerically integrate the above formula and study various properties of the EWCS  $E_w$ .

The left plot in Fig. 13 exhibits the EWCS as a function of separation scale  $D$  with fixed  $l = 1$  for different temperatures. It is obvious that the EWCS decreases with the

increase of  $D$  at first, and then, when  $D$  is beyond a certain critical value, the EWCS vanishes. This is expected, because MI vanishes and the subsystems disentangle. We also study the EWCS as a function of  $l$  with fixed  $D = 0.3$  in the right plot of Fig. 13, which shows that the

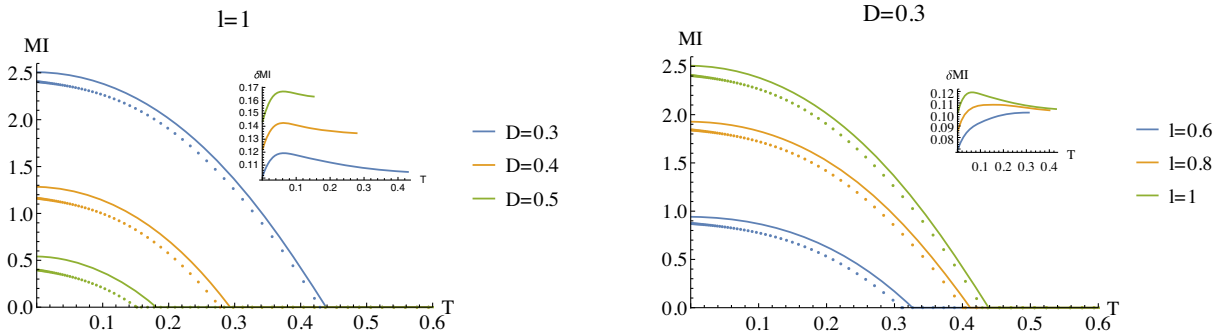


FIG. 10. MI as a function of the temperature for different  $l$  and  $D$ . The solid lines are for the Gubser-Rocha model, and the dotted lines are for the RN-AdS background. The inset plot describes the difference  $\delta MI$  as a function of  $T$  between the Gubser-Rocha model and the RN-AdS background.

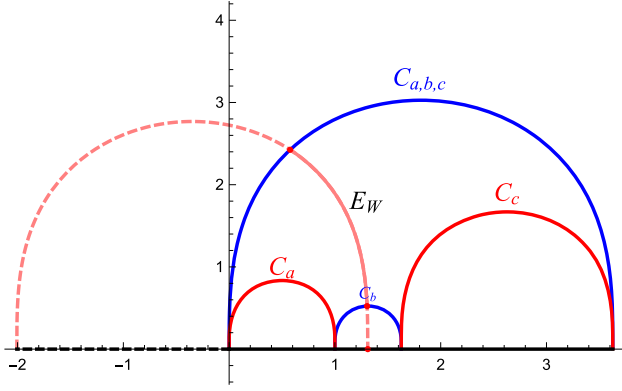


FIG. 11. The diagram of MI and  $E_W$  for a nonsymmetric configuration.

EWCS decreases with the decrease of  $l$  and vanishes when  $l$  is below some value. At the same time, we show EWCS over a RN-AdS background as a function of separation scale  $D$  with fixed  $l = 1$  for different temperatures (dashed lines). We find that, in contrast to the MI behavior, the EWCS of the Gubser-Rocha model is always smaller than that of the RN-AdS model. This shows that the MI reveals

the opposite entanglement property from that of the EWCS. For subsystems with the same temperature and configuration, EWCS shows that the dual quantum system of RN-AdS entangles more strongly than that of the Gubser-Rocha model, while MI gives the completely opposite conclusion. We hope that we can give a good understanding of this difference between the Gubser-Rocha model and the RN-AdS background from these two informational quantities in the future.

The temperature dependence of EWCS over Gubser-Rocha model is also explored in Fig. 14. We find that as the temperature rises, the EWCS slowly decreases, and then, when the temperature is beyond some critical value, the EWCS suddenly falls to zero. This is because the corresponding MI vanishes and means that both subsystems are disentangled. For comparison, we also show the temperature dependence of EWCS over a RN-AdS background, which is exhibited by dashed lines in Fig. 14. Again, this confirms the observation that the EWCS of the Gubser-Rocha model is always smaller than that of the RN-AdS model.

Next, we briefly discuss the EWCS for nonsymmetric configurations, for which EWCS is no longer the integral between the two turning points of the subsystems (see

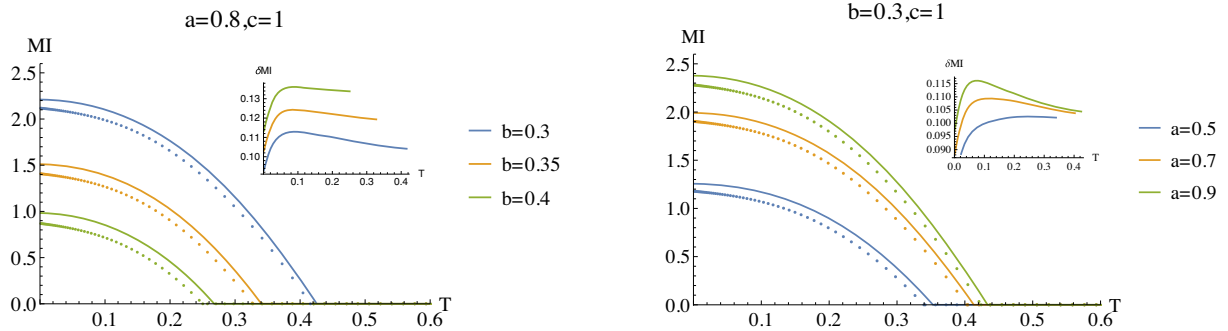


FIG. 12. MI as a function of the temperature for a nonsymmetrical configuration. The solid lines are for the Gubser-Rocha model, and the dotted lines are for the RN-AdS background.

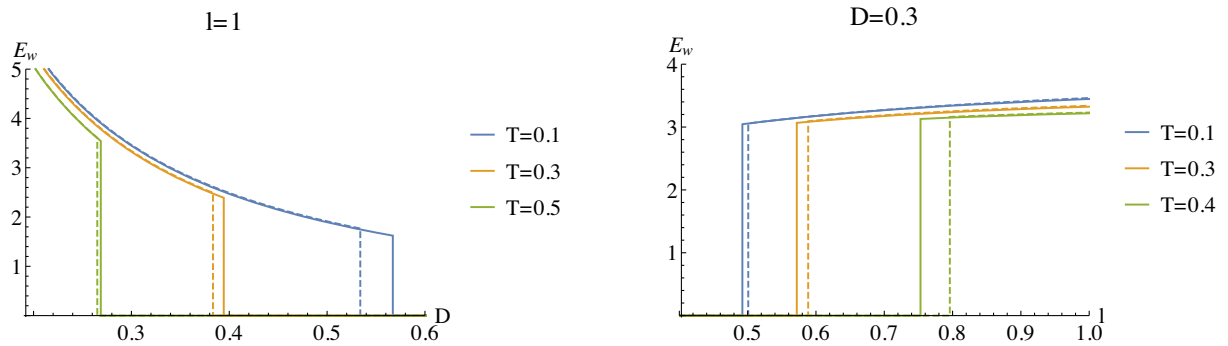


FIG. 13. Left plot: EWCS as a function of separation scale  $D$  with fixed system size  $l = 1$  for different temperatures. Right plot: EWCS as a function of system size  $l$  with fixed separation scale  $D = 0.3$  for different temperatures. The solid lines are for the Gubser-Rocha model, and the dashed lines are for the RN-AdS background.

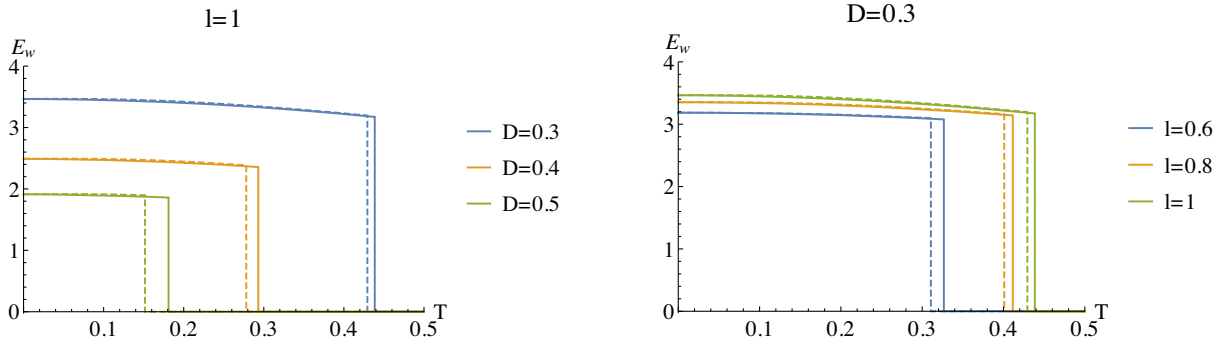


FIG. 14. EWCS as a function of temperature  $T$  with symmetric configuration. The left plot is for different separation sizes  $D$  and the fixed system size  $l = 1$ . The right plot is for different system sizes  $l$  and the fixed separation scale  $D = 0.3$ . The solid lines are for the Gubser-Rocha model, and the dashed lines are for the RN-AdS background.

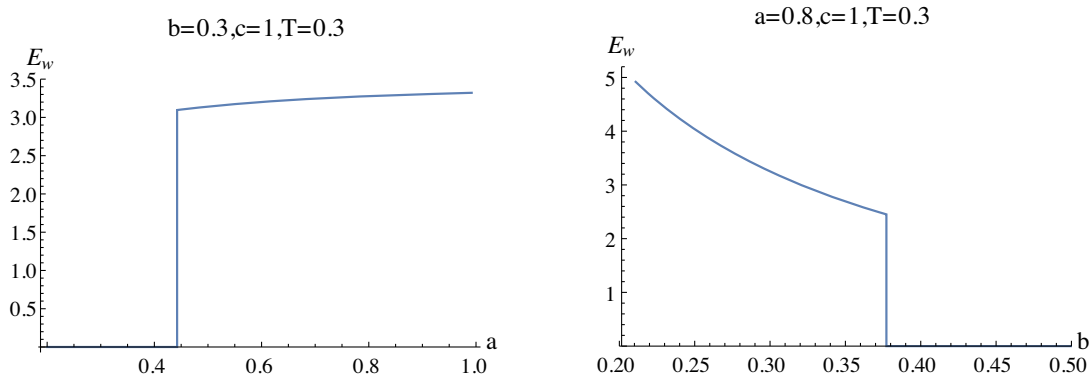


FIG. 15. EWCS as a function of the subsystem size  $a$  (left plot) and the separation size  $b$  (right plot).

Fig. 11). The calculation of the EWCS for a nonsymmetric configuration is hard work, in particular for low temperature. Reference [44] provides a detailed description on the numerical technics. We shall follow the method provided in Ref. [44] to work out the EWCS for a nonsymmetric configuration. We sum up the results as follows:

- (1) When the subsystem size becomes small or the separation size becomes large, both the subsystems disentangle (Fig. 15). In the entangling region,

EWCS monotonically increases (decreases) as the subsystem size (separation size) increases (Fig. 15).

- (2) In the high-temperature region, the subsystems are disentangling. In the intermediate-temperature region, as the temperature rises, the EWCS monotonically decreases (Fig. 16). These observations are consistent with those in other models—for example, for the RN-AdS background [44] and the holographic model with momentum relaxation [45,46].

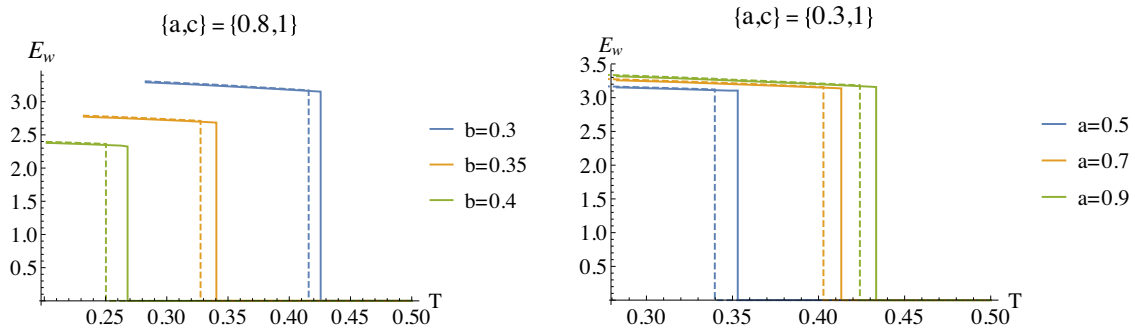


FIG. 16. EWCS as a function of temperature for a nonsymmetric configuration. The solid lines are for the Gubser-Rocha model, and the dotted lines are for the RN-AdS background.

(3) The EWCS of the Gubser-Rocha model is also smaller than that of the RN-AdS model (see Fig. 16). The above results for a nonsymmetric configuration are consistent with that for symmetric configuration.

Before closing this section, we argue that the EWCS can be a better diagnostic tool than the HEE and MI. First, EE cannot recognize the fact that the direct product state is entangled, so it is not suitable to be used as a measure of the entanglement of mixed states. Meanwhile, MI seems to be a better measure of the entanglement of mixed states, because it can obtain a value for the direct product state. However, it should be noted that since the definition of MI is directly related to EE (in fact, MI is a combination of EE), it can be expected that in some cases, MI can be directly derived from the behavior of EE. In this paper, Fig. 4 shows that the HEE presents a singular nonmonotonic behavior at very low temperature. As a result, the MI in Fig. 12 also shows some obvious nonmonotonic behaviors. Moreover, the nonmonotonic behavior of MI is just opposite to that of HEE. This is because the dominant term of the behavior with temperature in the definition of MI is  $S_{AB}$ , so the nonmonotonic behavior of MI is opposite to HEE. In fact, the key of these nonmonotonic behaviors of HEE and MI comes from the singular properties of IR fixed points of the Einstein-Maxwell-dilaton gravity theory in consideration. The definition of EWCS shows that it connects two surfaces in the entanglement wedge, so it is unlikely to be controlled by HEE, the minimum surface ending on the AdS boundary. In other words, it can capture information distinct from HEE. Moreover, EWCS can also identify the zero entanglement of the direct product state. Therefore, EWCS not only has no dependence on HEE, but it also has the ability to recognize the zero entanglement of the direct product states. Furthermore, it can be seen from Figs. 14 and 16 that EWCS does not show the same nonmonotonicity as HEE and MI in the zero-temperature limit. This verifies the observation that there is no dependency between HEE and EWCS. In this sense, EWCS can be a better measure of entanglement of mixed states than EE and MI.

#### IV. CONCLUSION AND DISCUSSION

In this paper, we study the information quantities, including HEE, MI, and EWCS, over the Gubser-Rocha model. The informational quantities from the Gubser-Rocha model exhibit some common characteristics of most holographic models. We summarize these properties as follows:

- (1) As the subsystem size enlarges, both MI and EWCS monotonically decrease, and then when the subsystem size is beyond certain critical value, MI and EWCS drop down to zero, and so the subsystems disentangle.
- (2) When the separation size is small, the subsystems disentangle. As the separation size increases beyond

a certain critical value, both MI and EWCS have nontrivial values. While the separation size is further enlarged, both MI and EWCS monotonically increase.

- (3) In the high-temperature region, both MI and EWCS monotonically decrease as the temperature climbs up, and then when the temperature exceeds some critical value, MI and EWCS drop down to zero and a disentangling phase transition happens.

In contrast to most holographic models such as a RN-AdS background with nonvanishing ground-state entropy density, the Gubser-Rocha model has vanishing ground-state entropy density. We expect that some novel, even singular informational properties in the limit of zero temperature emerges. However, we have not found any singular behavior of entanglement-related physical quantities in the zero-temperature limit. A brief comment is presented as follows: In an AdS-RN black hole system, the zero-temperature limit means  $\mu \rightarrow \sqrt{6}$ , where the metric and the scaling unit are both finite. Therefore, the HEE in the zero-temperature limit will approach a fixed value. However, the zero-temperature limit of the Gubser-Rocha model means  $Q \rightarrow \infty$  and hence  $\mu \rightarrow \infty$ , where the metric and the scaling unit are both infinite. The HEE behavior needs to be analyzed carefully. Interestingly,  $\mu \rightarrow \infty$  indicates that any strip with finite width  $l$  will have a vanishing  $\hat{l}$ . It seems that the minimum surface should reside in the near-boundary region, and the behavior of HEE seems to be determined by the AdS boundary. If this is true, the HEE will behave as  $S \sim -1/l$ , because in the AdS case we have  $\hat{S} \sim -1/\hat{l}$ , and hence we obtain  $S = \hat{S}/\mu \sim -1/(\mu\hat{l}) \sim -1/l$ . However, this expectation is not true, because the zero-temperature limit for the Gubser-Rocha model also renders the metric divergent.

Nevertheless, we found a peculiar property of these entanglement-related physical quantities of the Gubser-Rocha model: that the HEE in the low-temperature region decreases with the increase of temperature, which is contrary to the entanglement property of most holographic models. We argued that this novel phenomenon results from the singular property of the Gubser-Rocha model in the limit of zero temperature.

We also found that the HEE, as well as the MI, of the Gubser-Rocha model is larger than that of the RN-AdS model; meanwhile, the EWCS of the Gubser-Rocha model is smaller than that of the RN-AdS model. This result suggests that the EWCS exhibits distinct behaviors from the HEE as well as the MI. By comparing the definitions of HEE, MI, and EWCS and their numerical behaviors, we can find that EWCS has different behaviors from HEE and MI, and is more suitable for measuring the entanglement of mixed states.

Several directions deserve further study and promotion. First of all, whether MI or EWCS is more suitable for describing the mixed-state entanglement is worth

discussing in more holographic models. Second, the ground state with vanishing entropy density can be constructed based on the Gubser-Rochas model, so it is worthwhile to explore the mixed-state entanglement of ground states in these generalized models. Third, more mixed-state entanglement, such as Renyi entropy or entanglement negativity, could be considered in this model and further compared with HEE, MI, and EWCS. Fourth, as a supplement and confirmation of our numerical results, we can also analytically study the related informational quantities in different regions, especially the high/low-temperature limit and the limit of a large/small system scale or separated scale, following the studies in Refs. [34,58–60]. Finally, we can also study the nonequilibrium dynamics of related informational quantities to reveal more interesting properties of our model and further examine more inequalities of MI, EWCS, or reflected entropy. Lots of works along this direction have been done; see Refs. [61–63] and references therein.

### ACKNOWLEDGMENTS

This work is supported by the Natural Science Foundation of China under Grants No. 11775036, No. 11905083, No. 11847055, No. 11705161 and by the Fok Ying Tung Education Foundation under Grant No. 171006. Guoyang Fu is supported by the Postgraduate Research & Practice Innovation Program of Jiangsu Province (No. KYCX20\_2973). Jian-Pin Wu is also supported by the Top Talent Support Program from Yangzhou University.

### APPENDIX: THE METHOD OF CALCULATING HEE

In this appendix, we derive the expression of HEE in the static homogeneous background in general as

$$ds^2 = g_{tt}(z)dt^2 + g_{zz}(z)dz^2 + g_{xx}(z)dx^2 + g_{yy}(z)dy^2. \quad (\text{A1})$$

The induced metric of the minimal surface  $\gamma_A$  has the form

$$ds_{ind}^2 = (g_{zz}z'(x) + g_{xx})dx^2 + g_{yy}dy^2. \quad (\text{A2})$$

Since the configuration is an infinitely long strip in the dual boundary (see Fig. 1), the area of  $\gamma_A$  can be expressed as

$$\text{Area}(\gamma_A) = \iint \sqrt{g_{yy}(z)(g_{xx}(z) + z'(x)^2g_{zz}(z))} dx dy, \quad (\text{A3})$$

where  $z'(x) = dz/dx$ . Because the minimal surface  $\gamma_A$  is invariant along the  $y$  direction, we can integrate out  $y$ . And then, after ignoring several common factors, the HEE can be expressed as

$$\hat{S} = \int_0^{\hat{l}} \sqrt{g_{yy}(z)(g_{xx}(z) + z'(x)^2g_{zz}(z))} dx. \quad (\text{A4})$$

We see that the HEE can be described by  $z(x)$ , which is geodesic in the bulk spacetime.

To solve  $z(x)$ , usually we can treat Eq. (A4) as an action and vary it, and we obtain the Euler-Lagrange equation as

$$\begin{aligned} & 2g_{yy}g_{zz}z'(x)^2g'_{xx} \\ & + g_{xx}[g_{yy}(-2g_{zz}z''(x) - z'(x)^2g'_{zz} + g'_{xx}) \\ & + g_{zz}z'(x)^2g'_{yy}] + g_{xx}^2g'_{yy} = 0. \end{aligned} \quad (\text{A5})$$

We can numerically solve the above equation by the shoot method or the relaxation method. For the shoot method, we first assume a set of initial conditions and then adjust the initial conditions until the shooting point matches the aim point. The relaxation method is the better one. The differential equation can be replaced by finite difference equations on a discrete set of points, and then we can obtain the solution by iteration. For detailed discussions, we can refer to Refs. [64–67].

For the static case, there is a simpler way to obtain the HEE. When we treat Eq. (A4) as an action, one has the corresponding Hamiltonian, which is given by

$$\mathcal{H} = \frac{\partial \mathcal{L}}{\partial z'(x)} z'(x) - \mathcal{L}, \quad (\text{A6})$$

where the Lagrange is

$$\mathcal{L} = \sqrt{g_{yy}(z)(g_{xx}(z) + z'(x)^2g_{zz}(z))}. \quad (\text{A7})$$

Because of the Hamiltonian conservation, we can obtain

$$z'(x) = \frac{\sqrt{g_{xx}(z)}\sqrt{g_{xx}(z)g_{yy}(z) - g_{xx}(z_*)g_{yy}(z_*)}}{\sqrt{g_{xx}(z_*)g_{yy}(z_*)g_{zz}(z)}}, \quad (\text{A8})$$

where we have used the condition  $dz/dx|_{z=z_*} = 0$ . From the above equation, the length  $\hat{l}$  can be obtained in terms of  $z_*$ :

$$\frac{\hat{l}}{2} = \int_{\epsilon}^{z_*} dz \frac{\sqrt{g_{xx}(z_*)g_{yy}(z_*)g_{zz}(z)}}{\sqrt{g_{xx}(z)}\sqrt{g_{xx}(z)g_{yy}(z) - g_{xx}(z_*)g_{yy}(z_*)}}. \quad (\text{A9})$$

Then, the HEE can be expressed as

$$\hat{S} = \int_{\epsilon}^{z_*} dz \frac{g_{xx}(z)g_{yy}(z)\sqrt{g_{zz}(z)}}{\sqrt{g_{xx}(z)(g_{xx}(z)g_{yy}(z) - g_{xx}(z_*)g_{yy}(z_*))}}. \quad (\text{A10})$$

Therefore, the HEE can be obtained by a direct numerical integration using `NDSolve` in *Mathematica*, which is the

way we used in this paper. This trick bypasses the explicit solution  $z(x)$ . Before closing this section, we would like to emphasize that given the  $z_*$  in the region  $(0,1)$ , we can

obtain the length  $\hat{l}$  by a direct numerical integration. Conversely, we can also give any value of the  $z_*$  corresponding to some  $\hat{l}$ .

- 
- [1] J. M. Maldacena, The large- $N$  limit of superconformal field theories and supergravity, *Int. J. Theor. Phys.* **38**, 1113 (1999); *Adv. Theor. Math. Phys.* **2**, 231 (1998).
- [2] S. S. Gubser, I. R. Klebanov, and A. M. Polyakov, Gauge theory correlators from noncritical string theory, *Phys. Lett. B* **428**, 105 (1998).
- [3] E. Witten, Anti-de Sitter space and holography, *Adv. Theor. Math. Phys.* **2**, 253 (1998).
- [4] O. Aharony, S. S. Gubser, J. M. Maldacena, H. Ooguri, and Y. Oz, Large- $N$  field theories, string theory and gravity, *Phys. Rep.* **323**, 183 (2000).
- [5] J. M. Maldacena, Eternal black holes in anti-de Sitter, *J. High Energy Phys.* **04** (2003) 021.
- [6] M. Van Raamsdonk, Building up spacetime with quantum entanglement, *Gen. Relativ. Gravit.* **42**, 2323 (2010); *Int. J. Mod. Phys. D* **19**, 2429 (2010).
- [7] M. Van Raamsdonk, Building up spacetime with quantum entanglement II: It from BC-bit, [arXiv:1809.01197](https://arxiv.org/abs/1809.01197).
- [8] J. Maldacena and L. Susskind, Cool horizons for entangled black holes, *Fortschr. Phys.* **61**, 781 (2013).
- [9] T. Takayanagi, Holographic spacetimes as quantum circuits of path-integrations, *J. High Energy Phys.* **12** (2018) 048.
- [10] S. Ryu and T. Takayanagi, Holographic Derivation of Entanglement Entropy from AdS/CFT, *Phys. Rev. Lett.* **96**, 181602 (2006).
- [11] T. Takayanagi, Entanglement entropy from a holographic viewpoint, *Classical Quantum Gravity* **29**, 153001 (2012).
- [12] A. Lewkowycz and J. Maldacena, Generalized gravitational entropy, *J. High Energy Phys.* **08** (2013) 090.
- [13] V. E. Hubeny, M. Rangamani, and T. Takayanagi, A covariant holographic entanglement entropy proposal, *J. High Energy Phys.* **07** (2007) 062.
- [14] X. Dong, A. Lewkowycz, and M. Rangamani, Deriving covariant holographic entanglement, *J. High Energy Phys.* **11** (2016) 028.
- [15] M. Headrick and T. Takayanagi, A holographic proof of the strong subadditivity of entanglement entropy, *Phys. Rev. D* **76**, 106013 (2007).
- [16] A. C. Wall, Maximin surfaces, and the strong subadditivity of the covariant holographic entanglement entropy, *Classical Quantum Gravity* **31**, 225007 (2014).
- [17] S. Ryu and T. Takayanagi, Aspects of holographic entanglement entropy, *J. High Energy Phys.* **08** (2006) 045.
- [18] H. Casini, M. Huerta, and R. C. Myers, Towards a derivation of holographic entanglement entropy, *J. High Energy Phys.* **05** (2011) 036.
- [19] M. Rahimi, M. Ali-Akbari, and M. Lezgi, Entanglement entropy in a non-conformal background, *Phys. Lett. B* **771**, 583 (2017).
- [20] S. F. Lokhande, G. W. J. Oling, and J. F. Pedraza, Linear response of entanglement entropy from holography, *J. High Energy Phys.* **10** (2017) 104.
- [21] R. C. Myers and A. Singh, Comments on holographic entanglement entropy and RG flows, *J. High Energy Phys.* **04** (2012) 122.
- [22] Y. Ling, P. Liu, C. Niu, J. P. Wu, and Z. Y. Xian, Holographic entanglement entropy close to quantum phase transitions, *J. High Energy Phys.* **04** (2016) 114.
- [23] Y. Ling, P. Liu, and J. P. Wu, Characterization of quantum phase transition using holographic entanglement entropy, *Phys. Rev. D* **93**, 126004 (2016).
- [24] Y. Ling, P. Liu, J. P. Wu, and Z. Zhou, Holographic metal-insulator transition in higher derivative gravity, *Phys. Lett. B* **766**, 41 (2017).
- [25] A. Pakman and A. Parnachev, Topological entanglement entropy and holography, *J. High Energy Phys.* **07** (2008) 097.
- [26] X. M. Kuang, E. Papantonopoulos, and B. Wang, Entanglement entropy as a probe of the proximity effect in holographic superconductors, *J. High Energy Phys.* **05** (2014) 130.
- [27] I. R. Klebanov, D. Kutasov, and A. Murugan, Entanglement as a probe of confinement, *Nucl. Phys.* **B796**, 274 (2008).
- [28] S. J. Zhang, Holographic entanglement entropy close to crossover/phase transition in strongly coupled systems, *Nucl. Phys.* **B916**, 304 (2017).
- [29] X. X. Zeng and L. F. Li, Holographic phase transition probed by nonlocal observables, *Adv. High Energy Phys.* **2016**, 1 (2016).
- [30] H. Guo, X. M. Kuang, and B. Wang, Holographic entanglement entropy and complexity in Stckelberg superconductor, *Phys. Lett. B* **797**, 134879 (2019).
- [31] H. Casini and M. Huerta, A finite entanglement entropy and the c-theorem, *Phys. Lett. B* **600**, 142 (2004).
- [32] M. M. Wolf, F. Verstraete, M. B. Hastings, and J. I. Cirac, Area Laws in Quantum Systems: Mutual Information and Correlations, *Phys. Rev. Lett.* **100**, 070502 (2008).
- [33] M. Headrick, Entanglement Renyi entropies in holographic theories, *Phys. Rev. D* **82**, 126010 (2010).
- [34] W. Fischler, A. Kundu, and S. Kundu, Holographic mutual information at finite temperature, *Phys. Rev. D* **87**, 126012 (2013).
- [35] B. Groisman, S. Popescu, and A. Winter, Quantum, classical, and total amount of correlations in a quantum state, *Phys. Rev. A* **72**, 032317 (2005).
- [36] T. Takayanagi and K. Umemoto, Entanglement of purification through holographic duality, *Nat. Phys.* **14**, 573 (2018).

- [37] P. Nguyen, T. Devakul, M. G. Halbasch, M. P. Zaletel, and B. Swingle, Entanglement of purification: From spin chains to holography, *J. High Energy Phys.* **01** (2018) 098.
- [38] N. Bao and I.F. Halpern, Conditional and multipartite entanglements of purification and holography, *Phys. Rev. D* **99**, 046010 (2019).
- [39] K. Umemoto and Y. Zhou, Entanglement of purification for multipartite states and its holographic dual, *J. High Energy Phys.* **10** (2018) 152.
- [40] J. Kudler-Flam and S. Ryu, Entanglement negativity and minimal entanglement wedge cross sections in holographic theories, *Phys. Rev. D* **99**, 106014 (2019).
- [41] S. Dutta and T. Faulkner, A canonical purification for the entanglement wedge cross-section, *J. High Energy Phys.* **03** (2021) 178.
- [42] Y. Kusuki, J. Kudler-Flam, and S. Ryu, Derivation of Holographic Negativity in  $\text{AdS}_3/\text{CFT}_2$ , *Phys. Rev. Lett.* **123**, 131603 (2019).
- [43] R. Q. Yang, C. Y. Zhang, and W. M. Li, Holographic entanglement of purification for thermofield double states and thermal quench, *J. High Energy Phys.* **01** (2019) 114.
- [44] P. Liu, Y. Ling, C. Niu, and J. P. Wu, Entanglement of purification in holographic systems, *J. High Energy Phys.* **09** (2019) 071.
- [45] Y. f. Huang, Z. j. Shi, C. Niu, C. y. Zhang, and P. Liu, Mixed state entanglement for holographic axion model, *Eur. Phys. J. C* **80**, 426 (2020).
- [46] M. Ghodrati, X. M. Kuang, B. Wang, C. Y. Zhang, and Y. T. Zhou, The connection between holographic entanglement and complexity of purification, *J. High Energy Phys.* **09** (2019) 009.
- [47] S. S. Gubser and F. D. Rocha, Peculiar properties of a charged dilatonic black hole in  $\text{AdS}_5$ , *Phys. Rev. D* **81**, 046001 (2010).
- [48] J. Ren, Quantum phase transitions of charged Renyi entropies from hyperbolic black holes, *J. High Energy Phys.* **05** (2021) 080.
- [49] H. S. Jeong, K. Y. Kim, Y. Seo, S. J. Sin, and S. Y. Wu, Holographic spectral functions with momentum relaxation, *Phys. Rev. D* **102**, 026017 (2020).
- [50] J. P. Wu, Some properties of the holographic fermions in an extremal charged dilatonic black hole, *Phys. Rev. D* **84**, 064008 (2011).
- [51] W. J. Li, R. Meyer, and H. b. Zhang, Holographic non-relativistic fermionic fixed point by the charged dilatonic black hole, *J. High Energy Phys.* **01** (2012) 153.
- [52] Y. Ling, C. Niu, J. P. Wu, and Z. Y. Xian, Holographic lattice in Einstein-Maxwell-dilaton gravity, *J. High Energy Phys.* **11** (2013) 006.
- [53] M. Alishahiha, M. R. Mohammadi Mozaffar, and A. Molabashi, Holographic aspects of two-charged dilatonic black hole in  $\text{AdS}_5$ , *J. High Energy Phys.* **10** (2012) 003.
- [54] S. S. Gubser and I. Mitra, The evolution of unstable black holes in anti-de Sitter space, *J. High Energy Phys.* **08** (2001) 018.
- [55] C. P. Herzog, I. R. Klebanov, S. S. Pufu, and T. Tesileanu, Emergent quantum near-criticality from baryonic black branes, *J. High Energy Phys.* **03** (2010) 093.
- [56] K. Goldstein, S. Kachru, S. Prakash, and S. P. Trivedi, Holography of charged dilaton black holes, *J. High Energy Phys.* **08** (2010) 078.
- [57] J. Molina-Vilaplana and P. Sodano, Holographic view on quantum correlations and mutual information between disjoint blocks of a quantum critical system, *J. High Energy Phys.* **10** (2011) 011.
- [58] S. Kundu and J. F. Pedraza, Aspects of holographic entanglement at finite temperature and chemical potential, *J. High Energy Phys.* **08** (2016) 177.
- [59] K. Babaei Velni, M. R. Mohammadi Mozaffar, and M. H. Vahidinia, Some aspects of entanglement wedge cross-section, *J. High Energy Phys.* **05** (2019) 200.
- [60] W. Fischler and S. Kundu, Strongly coupled gauge theories: High and low temperature behavior of non-local observables, *J. High Energy Phys.* **05** (2013) 098.
- [61] K. Babaei Velni, M. R. Mohammadi Mozaffar, and M. H. Vahidinia, Evolution of entanglement wedge cross section following a global quench, *J. High Energy Phys.* **08** (2020) 129.
- [62] Y. T. Zhou, X. M. Kuang, Y. Z. Li, and J. P. Wu, Holographic subregion complexity under a thermal quench in an Einstein-Maxwell-axion theory with momentum relaxation, *Phys. Rev. D* **101**, 106024 (2020).
- [63] Y. T. Zhou, M. Ghodrati, X. M. Kuang, and J. P. Wu, Evolutions of entanglement and complexity after a thermal quench in massive gravity theory, *Phys. Rev. D* **100**, 066003 (2019).
- [64] C. Ecker, Entanglement entropy from numerical holography, [arXiv:1809.05529](https://arxiv.org/abs/1809.05529).
- [65] C. Ecker, D. Grumiller, W. van der Schee, M. M. Sheikh-Jabbari, and P. Stanzer, Quantum Null Energy Condition and its (non)saturation in 2d CFTs, *SciPost Phys.* **6**, 036 (2019).
- [66] C. Ecker, J. Erdmenger, and W. Van Der Schee, Non-equilibrium steady state formation in 3 + 1 dimensions, [arXiv:2103.10435](https://arxiv.org/abs/2103.10435).
- [67] C. Ecker, D. Grumiller, H. Soltanpanahi, and P. Stanzer, QNEC2 in deformed holographic CFTs, *J. High Energy Phys.* **03** (2021) 213.